Deflagration-to-detonation transition in porous energetic materials: A comparative model study

SHAOJIE XU and D. SCOTT STEWART
Theoretical and Applied Mechanics, University of Illinois, Urbana, USA

Abstract. A numerical study of deflagration-to-detonation transition (DDT) in porous HMX materials is carried out. Three reactive-flow models varying from single phase to three phase formulations are chosen for the study. The GISPA model is a single-phase model and the BKS model is a simplified two-phase, gas and solid model. The SVG model is a three-phase model which is based on evolution of solid, gas and void. The modeling assumptions made in construction of the SVG model are presented with a brief description of the other two models. In addition to hydrodynamic modeling, a new reaction-kinetics model, or rate law, is presented to model energy release. The rate law accounts for autocatalytic decomposition of HMX and the pressure dependent shock-to-detonation transition kinetics. The model results are compared in detail against the DDT events observed in physical experiments. Numerical simulation of inert compaction waves and DDT is carried out for parameters suitable for powered HMX. The simulation shows that all three models can effectively predict: (a) the formation of secondary compaction wave and a high-density plug, (b) initiation of the transition to detonation in the front of the plug, and (c) survival of the plug residual after the detonation. The SVG model compares the best against the measurable data of the physical experiment and is also computationally efficient and well-posed. Therefore it is a good candidate for multi-dimensional DDT calculations.

Key words: energetic materials, deflagration, detonation, porous materials

1. Introduction

Over approximately the past twenty-five years, a number of investigators have developed engineering models in order to describe deflagration, detonation and deflagration-to-detonation transition models (DDT) in porous energetic materials. We distinguish them as *engineering* models as opposed to a *standard* model, because unlike *standard models* whose mathematical formulation enjoy consensus amongst researchers and whose predictions confirm the outcome of widely varying classes of experiments, *engineering models* have formulations that are less certain, in debate and have less ability to predict experiments. However, engineering models are utilized widely at the present time to predict events in porous energetic materials such as damaged propellants and explosive powders, because of the technological importance of these materials. It has been essential to invent and improve the engineering models and try to bring them to a higher level of scientific certainty.

A goal of current study is to establish an engineering model for the purpose of multi-dimensional DDT simulations. The multiple time and length scales that are needed to describe DDT phenomena presents an inherent difficulty for reactive-flow calculations. Stability of the numerical algorithms used to solve the models usually requires that small time steps be used. Hence, large run times and memory allocations are required. The computational requirements are the most demanding in complex geometries. A way to alleviate the computational burden is to develop a model with the simplest mathematical structure that is physically sound and makes predictions consistent with the experiments.

In this paper we describe a comparative study of the properties of three such engineering models that are capable of predicting DDT in a one-dimensional tube geometry for a representative porous energetic material, granular HMX. The three models are Bdzil-Kapila-Stewart (BKS) model, gas-interpolated solid Stewart-Asay-Prasad (GISPA) model and solid-gas-void (SVG) model. The purpose of the study is to examine the differences in the predictions among the three models that have distinct structural differences in their formulation, but at the same time share great similarities. The BKS model is an asymptotic reduction of the Baer-and-Nunziato (BN) model [1] under an assumption of a large interphase drag coefficient. This physically based reduction leads to a single velocity, which greatly simplifies the mathematical structure of the models that are formulated by identifying phase properties independently for each material, such as the Powers–Stewart–Krier (PSK) model [2] and the BN model. With the single-velocity assumption, the SVG model is constructed by consideration of solid, void and gas phases separately, together with an independent description of compaction and reaction processes which is adopted from the work by Stewart *et al.* [3]. The GISPA model is a single-phase model, modified from the Stewart–Prasad–Asay (SPA) model [3].

The development of the two-phase reactive-flow model BKS and aspects of the SVG model was most heavily influenced by the works of Kuo and Summerfield [4], Baer and Nunziato [1], Butler and Krier [5], Powers, Stewart and Krier [2]. The BKS model originally posed by Bdzil, Kapila and Stewart, is summarized in [6] and is the model developed by the Los Alamos National Laboratory DDT-modeling group [7].

Recently Stewart *et al.* [3] posed a single-phase alternative, the SPA model, to the two-phase formulation. In their approach, they assumed that there was an equation of state (EOS) that described the material in terms of one-phase variables. For example, the internal energy is assumed to be a function of the pressure, density and two additional thermodynamic state variables that describe the state of compaction and the state of reaction of the material, respectively. Thus, the governing equation for such a model in one dimension can be given by the three equations of ordinary hydrodynamics that reflect conservation of mass, momentum and energy with two rate laws that describe the material time rate of change of the compaction and the reaction variables. Such a one-dimensional model has five equations and provides a minimalistic description. The original SPA model used a simple modification of an ideal equation of state. The GISPA model presented in this work employs a more sophisticated non-ideal equation of state and uses the reaction progress variable to interpolate from a porous solid EOS to a reacted gas EOS, resulting in a simple functional form for the internal energy of mixture, $e(p, \rho, \lambda, \phi)$.

The three models span a range from a two-phase model (BKS) that has separately identified of solid and gas to a single-phase model (GISPA) that describes bulk phase quantities (mixture quantities) and utilize independent thermodynamic state variables to describe compaction and reaction as separate processes. The third model SVG lies in between, which combines the two-phase features of the BKS model with the character of the GISPA model that allows one to consider compaction and reaction as independent processes. All three models are single-velocity models which assume that there is essentially no relative motion between the micro-structurally averaged gas and solid phases. The one-velocity assumption for sufficiently compacted (not loosely compacted) beds has been recently verified by experiments of Asay et al. and is described in [8].

To investigate the structural differences of the models in terms of their physical predictions and to make unambiguous intra-model comparisons, the philosophy adopted here is to provide equal information to each model through the specification of constitutive relations.

For example, we utilize the same compaction and reaction laws and equations of state (EOS) in all models. Mathematically, the structure of a model is determined by its governing partial differential equations (PDEs). Variation in the number of independent variables and its evolution equations will alter the model structure. For this reason, we allow the models to have only the PDEs that appear in their basic formulation and extra PDEs that might be added by augmenting the kinetic description of the reaction rate (say), or similar additions are prohibited. As a consequence, direct correspondences amongst state variables of the different models can be attained that are unambiguous. According to this principle, the reaction kinetics of the BN model (see [6] and [9]) which uses two PDEs to describe reaction progress and grain-surface temperature is not included in this study. This restriction affects the prediction of the BKS model as we will see in the discussion of the model simulations.

Prior to the intra-model comparisons, parameters in each model are calibrated to a well-defined experimental data, such as position-time loci of the lead compaction and detonation fronts and their speeds, etc., which will be presented in detail later in this paper. Predictions of each model are compared against the experimental results for the DDT-tube test and also for another two parametric studies where initial porosity of the bed and initial impact pressure are varied respectively, while all other parameters are fixed to their calibrated values. The parametric study is compared with the PoP-plot from the physical experiment [10].

The empirical data used in the calibrated is from the DDT-tube test carried out by McAfee et al at Los Alamos National Laboratory [11]. The experiments show that a typical transient in the DDT-tube experiment can be described as follows. First a mechanical impact or thermal stimulus generates a compaction wave that propagates as a decrease in the porosity and an increase in density in the material. The internal configuration change of the bulk material and interactions between grains initiate a weak energy release and are associated with pyrolysis and combustion amongst the energetic grains. A region of confined combustion near the piston expands and the outer boundary of the combustion region acts like a secondary piston and further compacts the material to near solid state (without porosity). This dense unreacted materials has been called a plug, since no gases can penetrate it. When the pressure in the plug rises above a critical value, shock-to-detonation transition occurs and a detonation forms at the boundary of the plug furthest from the combustion and closest to the unreacted material. Hence a dense unreacted plug residual is observed to survive well after the onset of detonation.

Reaction-kinetics modeling has been a focus of recent DDT studies. The simulation of the SPA model which employs a simple Arrhenius-type rate law [3] has shown all the dynamics features of the experiment save one: the detonation originates in the combustion region and not in the plug. The qualitative discrepancy about the location of the origin of the detonation predicted by the SPA model is attributed to the reaction-rate model is used for energy release. Specifically, the rate law was thermally sensitive, hence the detonation was born in the hottest region. Here we introduce a different energy-release rate law which is instead sensitive to the lead shock pressure in the dense plug. Reaction rates that are sensitive to the shock pressure are more commonly used in the shock-to-detonation transition (SDT) of condensed (full density) explosive. With this change, we find that the detonation shock initiates towards the front of the plug immediately after the lead shock and that the ignition sequence is consistent with the observations of the experiments. A recent study of augmented-kinetics modeling for the BKS model has been carried out in [12], where a reaction-progress-like variable and its evolution equation with a pressure-dependent rate function is employed to describe reaction. Because it involves the effect of pore size on the gas-phase combustion with a simple description of grain-surface temperature, the improved kinetics model is able to predict plug formation.

However, this addition of extra state variables violates the principle of equal and minimal information adopted for this study.

The outline of the paper is as follows. Section 2 gives an overview of the features of the experimental data of the composite HMX tube test that is used later to calibrate the models. Section 3 presents the conservation laws for the three models. The description of the constitutive relations, such as equation of state, source terms and kinetics modeling for the energy release are left to Section 4. In Section 5, we discuss the solutions of the models, including verification of the solutions and study of the inert compaction-wave structures and comparisons among the models. We also describe the calibration principles used to determine parameters in compaction and reaction-rate laws. The results of the DDT simulation for each model are presented for the model parameters that best fit the DDT experiment. We discuss the qualitatively and quantitative differences in the simulations of the models. As an interesting verification of our reaction-rate sub-models, we compare the simulation of run-to-detonation distance versus the input shock pressure (PoP-plot) for 100 % and 70 % HMX, and the results are compared with an experiment that shows the PoP-plot data for [10]. Also in Section 5, we show the results obtained by varying the initial porosity in the virgin material, impacted by a 100 m/sec piston, with all the other model parameters fixed. The conclusions are in Section 6.

2. Experimental data

To study systematically the behavior of granular explosives, composite DDT-tube experiment was conducted at LANL by McAfee *et al.* [11]. There are more than 10 shots in the composite experiment with slight variation in initial conditions from one shot to another. Class A HMX with a grain-size distribution of 10 to 100 μ, was used and the bed was packed to an initial density of 1·22 g/cc for each test, which is nearly 70 % of the initial homogeneous solid density, referred to as 70 % theoretical maximum density TMD. There were small variations of the tube diameters and burn chambers from shot to shot. The numbers, location and types of pins inserted along the side of the tube were varied in each test. A schematic diagram of the instrumentation of the experiment obtained from Asay is shown in Figure 1.

Figure 2 is a schematic diagram of DDT events in the time-distance plane taken from [11]. The left portion of Figure 2, shows the sequence in a time-distance plane and the right portion of the same figure shows the events at different times in the tube. The loaded bed is impacted by a piston, labeled p, traveling at 100 m/sec, that is driven by the expansion of combustion gases of HMX powder in a burn chamber. The motion of the piston generates a compaction wave, labeled c, in the porous material which transforms the bed from 70 % TMD to about 90 % TMD. After an induction-type delay, an ignition wave, labeled b, develops near the piston. It propagates into the 90 % TMD material left behind by the leading compaction wave. The burning front forms a virtual piston that further compacts the material. It is thought that stress waves, generated by the acceleration of the burning front, coalesce to form a second shock-like front, labeled s, in the 90 % TMD material. Density measurements show that behind the shock-like front, the bed is fully compacted to 100 % TMD. The region of the full density is called a 'plug'. The rear of the plug is labeled vp for virtual piston. The location of the high density plug is determined experimentally from radiographic measurements. The trajectory of the rear of the plug as well as the burning shock front is not known with much accuracy. As plug grows, pressure builds up rapidly and finally prompt shock initiation occurs near the leading edge of the plug and a detonation, labeled
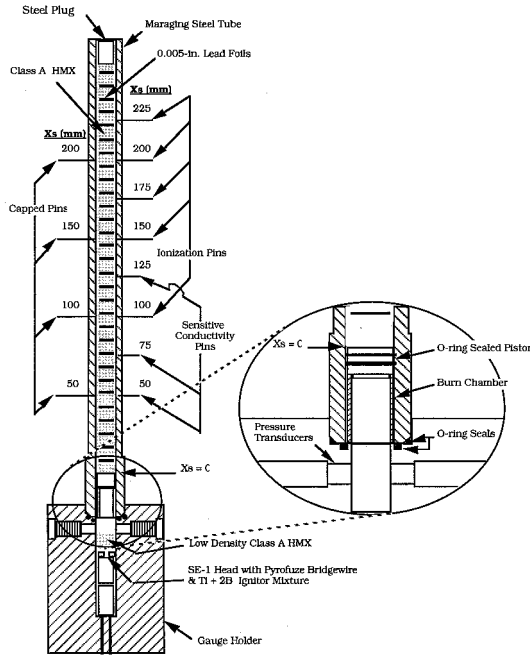
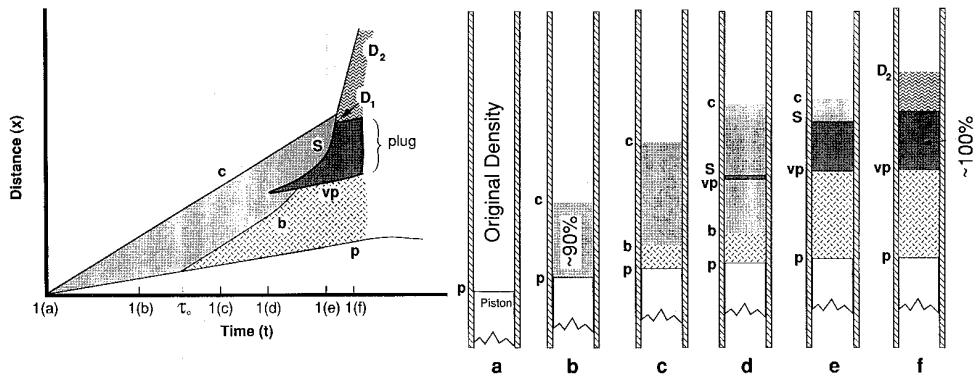*Figure 1.* Detailed drawing of the LANL-DDT tube.

Figure 2. Events of the LANL-DDT experiment. The left graph in time-distance plane shows schematically the loci detected in the LANL experiment and include: the piston path (b), the primary compaction wave (c), the secondary shock (S), the rear interface of the plug (vp) and the detonation wave (D). The right portion of the same figure shows the events at different times in the tube.

D, runs rapidly through the system. Figure 3 shows the experimental data from the LANL shot E-5586 obtained from McAfee *et al.* [11], displayed in a lab-frame space-time, characteristic plane. According to the description given above, we have labeled the various loci.

In order to compare the different predictions between models, we consider experiments where the initial porosity ψ is varied and all other conditions of the experiment are held fixed. Then for a fixed value of ψ, the length to detonation, or run distance X, from the end of the tube to the point of detonation is measured. Typically, the response is a U-shape: for a high value of porosity (low compaction) the run distance is longer; for intermediate values the run distance is a minimum, and for low values of porosity (high compaction) the run
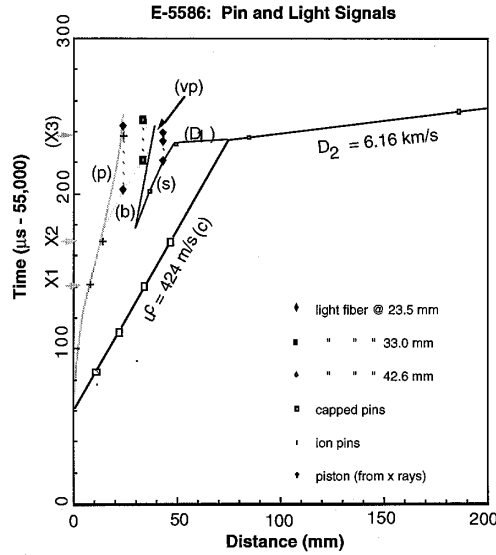
Figure 3. Experimental data from the LANL shot E-5586, obtained from McAfee etc. [11], displayed in a lab-frame space-time plane.

distance is longer again. A series of such experiments conducted by the Russian scientists Korotkov *et al.* [13] in PETN is representative of this behavior. Setup and instrumentation of the Russian experiments was similar to the LANL tests, but there was a difference in the means of ignition of the DDT tube. In particular, the steel tube filled with PETN powders was initiated by an electrically heated igniter. Unfortunately, extensive data for HMX powders is scarce or non-existent. So the comparison of the Russian data applied to HMX modeling is qualitative.

The porosity ψ in the Russian experiments is defined as the ratio of the pore volume V_{pore} to the total volume V of the charge

$$\psi = \frac{V_{\text{pore}}}{V} = \frac{V - V_{\text{solid}}}{V} = 1 - \frac{V_{\text{solid}}}{V} = 1 - \phi. \tag{1}$$

As reported in [13], ψ in their experiments varied from $0{\cdot}1$ to $0{\cdot}7$ for fine material with a particle size distribution centered on $20\ \mu$ diameter grains, and from $0{\cdot}05$ to $0{\cdot}5$ for coarse material with a particle-size distribution centered on $500\ \mu$ diameter grains. (Note that the higher values of ψ near $0{\cdot}7$ probably correspond to very loose materials. We cannot vouch for the accuracy of the reported experimentally values. But we have included this data due to the lack of any like data that we know of for HMX.) It is observed in DDT experiments that for very low initial density (high porosity), transition to detonation requires very large input energy in order to build up sufficient pressure in the compaction process, hence it is extremely difficult to conduct DDT experiments with very high porosity. For reliability, we use the data in [13] for $\psi \in (0{\cdot}1, 0{\cdot}6)$ with the average grain size of $20\ \mu$ in our parametric studies. Notice that in our comparison with the LANL data and between our models, we use the compaction variable ϕ to describe the state of the bed, instead of the porosity defined above, and the relation between the two is simply $\psi + \phi = 1$ or $\phi = 1 - \psi$. Figure 4, constructed from the data presented in [13], shows the length of pre-detonation run $X(\phi)$ plotted as a function of ϕ.
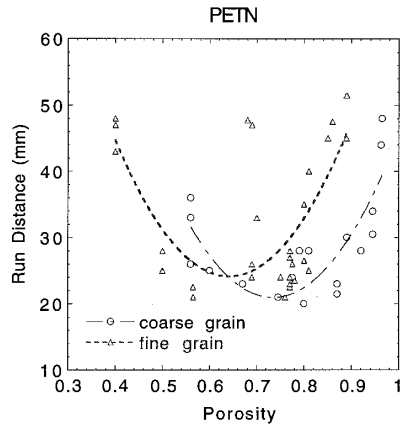
Figure 4. The run-to-detonation distance as a function of porosity in PETN from [13] shown for both coarse and fine grain PETN. (Data for porosity less than 0·4 are omitted.)

Compaction and detonation-wave structures were also presented in the description of the Russian experiments. From optical records that record space-time events, evidence of backward retonation can be found at nearly the same time that the forward propagation detonation occurs. The retonation propagates toward the effective piston into compressed, nearly solid material at speed, slower than that of the detonation. Similar transients can be found in the LANL data.

3. Model equations

The conservation laws for the three models BKS, SVG, and GISPA and their properties are presented in this section. The exact expressions for the various source terms and the EOS are discussed in Section 4 with associated constitutive laws.

3.1. CONSERVATION LAWS FOR THE BKS MODEL

The BKS models is a derivative of a two-phase model which was originated by Kuo and Summerfield and pursued by a number of investigators. Importantly, Kuo and Summerfield originated the idea of two phases, one for the gas and one for the solid, with separate and isolated equations of state to describe molecularly non-mixed phases of solids and gases. In particular, they assumed that there was an independent velocity for each phase and thay had equations for partial mass, momentum and energy of each of the phases. They suggested that the mixture equations should follow the global mixture rules laid out by the work of Truesdell and his co-workers. This approach led to a set of equations that were posed but not derived. A mature version of this approach, calibrated to solve DDT problems of the type discussed here, was presented by Baer and Nunziato [1]. Their model is dubbed BN.

The BKS model is a single-velocity symptotic reduction of the detailed BN model, derived in the limit of large interphase drag [7]. Experiments by Asay *et al.* [8] have shown that rapid gas permeation does not occur (hence indicating large interphase drag) for porosity less than 30 % in the experiment. Also on 100 μsec time-scale of the entire DDT event, the significant gas permeation in the bed is not an important interphase transfer mechanism for momentum. Thus a single-velocity model can be used. The BKS model was developed to

exploit this experimentally consistent simplification and to reduce formally the two-velocity, two-phase modeling principle by inclusion of the limit large interphase drag as measured by the dimensionless drag coefficient δ. In the asymptotic reduction worked out in [14], the velocity difference between the phases is a small quantity of order $1/\delta$, except in a thin shock-relaxation zone, where the velocity difference is of order one. The existence of such a shock-relaxation zone has been confirmed by a detailed numerical study of drag interaction between solid and gas phases, based on the BN model [15].

The one-velocity simplification not only reduces the number of evolution equations by one (only one momentum equation for mixture phase is needed), but also reduces the number of characteristics from six to three, which alleviates the difficulty in analysis on the mathematical structure of the solution. The system still remains hyperbolic, but cannot be written in a conservative formulation. This brings in difficulty in implementing modern numerical methods such as ENO schemes, since these high-order shock-capturing schemes generally require the system to be written in conservative form. Thus a *fix* to deal with the non-conservative form of the BKS model was required in order to make the computational problem well-posed and insensitive to the otherwise non-conservative shock structure. In particular, a shear-viscosity-like term was introduced and added to the pressure to force velocity equilibrium at the end of the relaxation zone [16]. The resulting BKS model can be summarized as the asymptotic reduction of the BN model with a viscosity regularization to eliminate the computationally ill-posed character of the numerics that otherwise would result. A series of studies have been done theoretically and numerically on the BKS model by Bdzil and Son [6] and Son [17] concerning the predictions of the shock structures and its end states. The studies show that the regularization procedure is apparently robust and leads to a workable numerical model.

The conservation laws for the BKS model are

$$\frac{\partial}{\partial t}(\phi_s \rho_s) + \frac{\partial}{\partial x}(\phi_s \rho_s u) = C_s^+, \tag{2}$$

$$\frac{\partial}{\partial t}(\phi_g \rho_g) + \frac{\partial}{\partial x}(\phi_g \rho_g u) = C_s^+, \tag{3}$$

$$\frac{\partial}{\partial t}(\phi u) + \frac{\partial}{\partial x}(\phi u^2 + p) = -\frac{\partial}{\partial x}\left(\mu \frac{\partial u}{\partial x}\right), \tag{4}$$

$$\frac{\partial}{\partial t}\left[\phi_s \rho_s \left(e_s + \frac{u^2}{2}\right)\right] + \frac{\partial}{\partial x}\left(u \phi_s \rho_s \left(e_s + \frac{u^2}{2}\right) + u \rho_s p_s\right)$$
$$= E_s^+ - \mu_s \frac{\partial}{\partial x}\left(\rho_s u \frac{\partial u}{\partial x}\right), \tag{5}$$

$$\frac{\partial}{\partial t}\left[\phi_g \rho_g \left(e_g + \frac{u^2}{2}\right)\right] + \frac{\partial}{\partial x}\left(u \phi_g \rho_g \left(e_g + \frac{u^2}{2}\right) + u \rho_g p_g\right)$$
$$= -E_s^+ - \mu_g \frac{\partial}{\partial x}\left(\rho_g u \frac{\partial u}{\partial x}\right), \tag{6}$$

$$\frac{\partial}{\partial t}(\rho \phi_s) + \frac{\partial}{\partial x}(\phi_s \rho u) = \rho \left(\mathcal{F} + \frac{C_s^+}{\rho_s}\right), \tag{7}$$
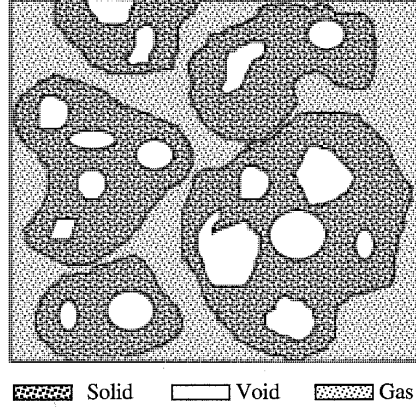
Solid ▢ Void ▨ Gas

Figure 5. Hypothetical microstructure assumed for the SVG mode, showing phases of solid, gas and void.

where C_s^+ and E_s^+ are phase exchange terms, μ_s, μ_g and $\mu = \phi_s \mu_s + \phi_g \mu_g$ are viscosity coefficients from the regularization. Notice that in the actual numerical implementation, a nonlinear viscosity form is employed which reduces viscosity in a smooth flow field [17]. The compaction rate function $\mathcal{F}$ is chosen to be

$$\mathcal{F} = k[p - p_0 - \mathcal{P}(\phi_s, P_h)], \tag{8}$$

where $\mathcal{P}$ is the configurational, or intergranular, stress and k is a rate constant which will be discussed later in Section 4.

The definitions of the mixture or bulk-phase quantities which obey mixture rules so that the overall equations obey the continuum conservation laws, are

$$\rho = \phi_s \rho_s + \phi_g \rho_g, \qquad p = \phi_s p_s + \phi_g p_g, \qquad e = (\phi_s \rho_s e_s + \phi_g \rho_g e_g)/\rho, \tag{9}$$

with saturation condition $\phi_s + \phi_g = 1$ and pure-phase equations of state

$$e_s = e_s(\rho_s, p_s), \qquad e_g = e_g(\rho_g, p_g). \tag{10}$$

The energy-exchange term has the following form

$$E_s^+ = \frac{u}{\rho} \left[(\phi_g \rho_g) \frac{\partial}{\partial x}(\phi_s p_s) - (\phi_s p_g) \frac{\partial}{\partial x}(\phi_g p_g) \right]$$

$$+ \left[\phi_s \rho_s \left(e_s + \frac{u^2}{2} \right) \right] C_s^+ - \{ (p_s - \mathcal{P}(\phi_s, P_h))\mathcal{F} + (t_s - t_g)H \} \tag{11}$$

where t_s and t_g are solid and gas-phase temperatures, respectively, and H is the interphase heat-transfer coefficient. In this study, we take $H = 0$ for simplicity.

3.2. CONSERVATION LAWS FOR THE SVG MODEL

We construct the SVG model by starting from the same continuum-mixture viewpoint that is at the origin of BKS, but with the addition of one additional phase, namely void. Thus, three independent phases are considered in the SVG model: solid, void and gas. For conceptual

purposes, we imagine that the void is confined to reside in pockets within a matrix of solid material. The gas is then thought to surround the porous solid and form a connected network. The gas phase outside the porous solid (comprise of solid with voids) is thought to be able to exert its pressure wholly on the porous solid, which in turn pushes back on the gas. Figure 5 shows a sketch of a hypothetical microstructure that reflects this physically-based *ansatz.* The SVG model really discusses the non-equilibrium processes between two phases, gas and porous solid, where the void fraction simply defines the properties of the porous solid, but nonetheless is an independent kinematic variable whose rate processes must be described. The void material itself has however no other physical properties. We are essentially neglecting the contributions of any gas trapped inside of solid and making the assumption that, at high enough pressure, gas escapes through fissures, etc., to connect with the surrounding gas phase by fracturing the porous solid. One has in mind a fluidized bed of porous solid surrounded by gas.

The evolution of each phase is described by its volume fraction variables

$$\phi_s = V_s/V, \qquad \phi_v = V_v/V, \qquad \phi_g = V_g/V, \qquad \phi_{ps} = V_{ps}/V = (V_s + V_v)/V, \quad (12)$$

where V_s, V_v, V_g and V_{ps} are respectively the solid, void, gas and porous solid volumes, where $V_{ps} = V_s + V_v$ and where V is total volume defined by $V = V_{ps} + V_g = V_s + V_v + V_g$. The saturation constraint relation $\phi_s + \phi_v + \phi_g = 1$ holds. We now assume that same mixture rules as the BKS model apply, for the density, pressure and the internal energy. If we consider the porous solid itself as a mixture of solid and void, we have expressions relating the density of the porous solid to the solid

$$\rho_{ps} = \frac{V_s}{V_s + V_v}\rho_s + \frac{V_v}{V_s + V_v}\rho_v = \frac{V_s}{V_s + V_v}\rho_s = \frac{\phi_s}{\phi_{ps}}\rho_s, \tag{13}$$

where $\rho_v = 0$ is applied. The mixture density can be expressed as

$$\rho = \phi_{ps}\rho_{ps} + \phi_g\rho_g = \phi_s\rho_s + \phi_g\rho_g. \tag{14}$$

Using the rule of the partial pressures similar to (13), we have the following relation for the pressure,

$$p_{ps} = \frac{\phi_s}{\phi_{ps}}p_s, \tag{15}$$

hence

$$p = \phi_{ps}p_{ps} + \phi_g p_g = \phi_s p_s + \phi_g p_g. \tag{16}$$

Note that expressions for the mixture pressure and density are exactly the same as for the BKS model. However a distinction is made between the solid pressure and the porous-solid pressure which are generally not the same. They are the same in the absence of void, *i.e.* $\phi_v = 0$. If both p_s and p_g were kept as independent phase variables, then two corresponding evolution equations would be needed, which would require a closure similar to that of the BKS model. For the SVG model however, we propose a different closure based upon pressure equilibrium. We assume that the pressure in the porous-solid phase equals pressure in the

surrounding gas phase, *i.e.* $p_{ps} = p_g$. Using the saturation constraint in (16), we are led to the second conclusion, namely that

$$p - p_g = p_{ps}. \tag{17}$$

Thus, the pressure-equilibrium closure assumes that the mixture pressure, the surrounding gas pressure, and the porous-solid pressure are all the same. When the void is absent, the model assumes that the porous-solid pressure is the solid pressure and equal to the gas pressure.

In such a two-phase model, exothermic chemical energy released from the mixture to supply the kinetic energy of motion, or recoverable energy stored in the mixture pressure, is associated with the differences in te internal energy of the solid and gas phases. Thus, it is important to keep two equations for the material time rate of change of the solid and gas-phase masses. We keep the same mass-conservation equations as used in BKS model with the single-velocity energy equation for the mixture results from the pressure-equilibrium closure. Finally, to complete the specification of the SVG model, we add two equations that describe the material time rate of change of ϕ_g (a reaction-like variable) and ϕ_v (a compaction-like variable).

Thus SVG has two mass-conservation equations written for the solid and the gas phase, respectively, one momentum equation and one energy equation both written for bulk variables. Similar to BKS, the SVG model is a hyperbolic system of six PDE's with three characteristic families. The SVG model equations are

$$\frac{\partial}{\partial t}(\phi_s \rho_s) + \frac{\partial}{\partial x}(\phi_s \rho_s u) = C_s^+, \tag{18}$$

$$\frac{\partial}{\partial t}(\phi_g \rho_g) + \frac{\partial}{\partial x}(\phi_g \rho_g u) = -C_s^+, \tag{19}$$

$$\frac{\partial}{\partial t}(\rho u) + \frac{\partial}{\partial x}(\rho u^2 + p) = 0, \tag{20}$$

$$\frac{\partial}{\partial r}\left[\rho\left(e + \frac{u^2}{2}\right)\right] + \frac{\partial}{\partial x}\left(u\left[\rho\left(e + \frac{u^2}{2}\right)\right] + u\rho p\right) = 0, \tag{21}$$

$$\frac{\partial}{\partial t}(\rho \phi_v) + \frac{\partial}{\partial x}(\phi_v \rho u) = \rho r_{\phi_v}, \tag{22}$$

$$\frac{\partial}{\partial t}(\rho \phi_g) + \frac{\partial}{\partial x}(\phi_g \rho u) = \rho r_{\phi_g}, \tag{23}$$

where the mixture rules and saturation constraint are

$$\rho = \phi_s \rho_s + \phi_g \rho_g, \qquad p = p_{ps} = p_g,$$
$$e = (\phi_s \rho_s e_s + \phi_g \rho_g e_g)/\rho, \phi_v + \phi_g + \phi_s = 1. \tag{24}$$

For the SVG model, we still use the individual equations of states for the solid and the gas following the two-phase modeling tradition

$$e_s = e_s(\rho_s, p_s), \qquad e_g = e_g(\rho_g, p_g). \tag{25}$$

3.3. CONSERVATION LAWS FOR THE GISPA MODEL

The SPA model was introduced in [3] as a single-phase model formulated only in terms of bulk quantities, but it retained independent state variables to describe the endothermic compaction process and the exothermic reaction processes. By use of an ideal form for the equation of state it was possible to reproduce almost all of the experimentally measured features of the LANL composite DDT-tube experiment. These included the compaction wave, the formation of a dense, reactionless plug, the secondary compaction wave, ignition and propagation of a detonation at the experimentally observed speed. The only qualitative aspects of the experiment that were not reproduced well by the original SPA model were that the detonation ignited in the hot region near the piston, rather than at the front of the secondary compaction wave and that no long-lived plug residual was observed in the simulation. The inability to simulate the plug residual in the experiment is attributed to the thermally sensitive kinetics used for the reaction rate.

There is analogy between the SVG and SPA models. In the SPA models, the compaction variable is taken to be ϕ and the complete compaction state is represented by $\phi = 1$. In the SVG model, the related compaction variable is the void fraction ϕ_v and when the material is completely compacted, $\phi_v = 0$. For both the SPA and SVG model, the compaction process is taken to be irreversible and once the complete compaction is reached, the compaction variable ceases to play any role in the model. Furthermore, both the SPA and SVG model have an independent reaction progress variable. In the SPA model, it is taken to be λ, where $\lambda = 1$ corresponds to complete reaction. In the SVG model, the reaction variable is ϕ_g and complete reaction is achieved when $\phi_g = 1$.

The SPA model uses an ideal equation of state as part of its constitutive relations, which affects its predictions for real materials. In order to remedy the deficiencies due to the simple ideal equation of state, a direct extension of SPA model to real materials is made in the GISPA model, which incorporates the non-ideal equation of state for HMX by a convex combination of solid-phase EOS and gas-phase EOS via the reaction progress variable λ. The solid phase is assumed to be a porous solid and an unreacted-solid equation of state is used for the porous solid, which is modified according to the Hermann and Carrol–Holt prescription for a porous EOS [18]. The compaction variable ϕ can be interpreted as the ratio of the solid volume to the porous-solid, thus an EOS for the porous solid can be obtained from the solid EOS $e_s(\rho, p)$ used in [18] by the modification: $e(p, \rho, \phi) \equiv e_s(\rho/\phi, p/\phi)$.

Hence, the mathematical structure of the GISPA model is the same as the SPA model, except that the EOS is non-ideal. It has three conservation laws for the mass, momentum and energy, plus two independent equations for compaction-state variable ϕ and reaction-state variable λ.

The governing equations for GISPA model are,

$$\frac{\partial}{\partial t}(\rho) + \frac{\partial}{\partial x}(\rho u) = 0, \tag{26}$$

$$\frac{\partial}{\partial t}(\rho u) + \frac{\partial}{\partial x}(\rho u^2 + p) = 0, \tag{27}$$

$$\frac{\partial}{\partial t}\left[\rho\left(e + \frac{u^2}{2}\right)\right] + \frac{\partial}{\partial x}\left(u\left[\rho\left(e + \frac{u^2}{2}\right)\right] + up\right) = 0, \tag{28}$$

$$\frac{\partial}{\partial t}(\rho\phi) + \frac{\partial}{\partial x}(u\phi) = \rho r_\phi, \tag{29}$$

$$\frac{\partial}{\partial t}(\rho\lambda) + \frac{\partial}{\partial x}(\rho u\lambda) = \rho r_\lambda, \tag{30}$$

We assume that the gas EOS is simply $e_g(p, \rho)$. Then the $e(p, \rho, \phi, \lambda)$ EOS is taken to be a simple weighted interpolation,

$$e(p, \rho, \phi, \lambda) = (1 - \lambda)e_s(\rho/\phi, p/\phi) + \lambda e_g(\rho, p). \tag{31}$$

(Functional forms for $e_s(\rho_s, p_s)$ and $e_g(\rho_g, p_g)$ are given in next section).

In summary, the BKS model is a two-phase, single-velocity, 6-equation model which is derived from an asymptotic reduction of the two-velocity, 7-equation BN model with a viscosity regularization. Th SVG is a 6-equation model with one velocity and three phases where one of the phases is void in that it has no mass and energy or strength, but occupies volume. Thus the SVG model has two phases, solid and gas, that define the mass, momentum and energy content which are affected by the presence of the void. The existence of the void phase affects the distribution of mass, momentum and energy between the solid and gas phases. The SVG model assumes pressure equilibrium between the porous solid and surrounding gas. The GISPA is a 5-equation model that conserves mass, momentum and energy for a single mixture phase. It assumes that compaction and reaction are independent thermodynamic processes that can be described by state variables such as ϕ and λ. We close the model by describing the material time rate of change of the variables that describe the two processes. In the next section, we describe the additional constitutive theory and functional forms that are needed to describe the non-ideal equation of state and to specify the reaction and compaction rates and other interphase exchange terms.

4. Constitutive theory

In this section we discuss the constitutive theory comprised of specification of the EOS and the compaction and reaction-rate functions for all three models. We adopt the same forms for consititutive theory where possible, in order to make unambiguous comparisons. The differences between the models are then partially recorded in the values of the parameters required to calibrate the simulations of the models to match the physical experiments of inert compaction and the LANL DDT-tube experiment

4.1. EQUATION OF STATE

A Helmholtz free-energy equation of state due to Hayes is assumed for full density, unreacted solid phase of HMX with the form

$$\begin{aligned}
e_s(p_s, \rho_s) &= \frac{1}{\Gamma}(p_s - p_{s0}) - \left(t_3 - \frac{p_{s0}}{\rho_{s0}}\right)\left(1 - \frac{\rho_{s0}}{\rho_s}\right) \\
&\quad + t_4\left\{\left(\frac{\rho_s}{\rho_{s0}}\right)^{n-1} - (n-1)\left[1 - \frac{\rho_{s0}}{\rho_s}\right] - 1\right\},
\end{aligned} \tag{32}$$

where t_3 and t_4 are defined as,

$$t_3 = C_{vs}T_{s0}\Gamma/\rho_{s0}, \qquad t_4 = H_1/(\rho_{s0}n(n-1)),$$

Table 1. Parameters used in the Hayes (solid) and the JWL (gas) EOS and ambient properties.

EOS Parameter	Value
H_1,(N/m^2)	$1 \cdot 3 \times 10^{10}$
n,	$9 \cdot 8$
R_1,	$4 \cdot 2$
R_2,	$1 \cdot 0$
ω,	$0 \cdot 25$
A,(N/m^2)	$[-8 \cdot 005 + 21 \cdot 39(\phi_{s0}\rho_0)10^{-3} - 16 \cdot 23(\phi_{s0}\rho_0)10^{-6} + 4 \cdot 595(\phi_{s0}\rho_0)10^{-9}]10^{11}$
B,(Nm^2)	$[-0 \cdot 014 + 0 \cdot 0349(\phi_{s0}\rho_0)10^{-3} + 0 \cdot 0156(\phi_{s0}\rho_0)10^{-6} - 0 \cdot 026(\phi_{s0}\rho_0)10^{-9}]10^{11}$
C_{vs},(N.m/kg/K$^\circ$),	$1 \cdot 5 \ 10^3$
C_{vg},(N.m/kg/K$^\circ$),	$[2 \cdot 4 - 0 \cdot 28((\phi_{s0}\rho_0)10^{-3} - 1 \cdot 3)]10^3$
Γ,(kg/m^3),	$2 \cdot 1 \ 10^3$
Q,(N.m),	$[7 \cdot 91 - 4 \cdot 33((\phi_{s0}\rho_0)10^{-3} - 1 \cdot 3)^2 - 0 \cdot 934((\phi_{s0}\rho_0)19^{-3} - 1 \cdot 3)]10^6$
p_{s0},(N/m^2),	$1 \cdot 0 \ 10^5$
p_{g0},(N/m^2),	$1 \cdot 0 \ 10^5$
T_{s0},(K$^\circ$),	300
T_{g0},(K$^\circ$),	300
ρ_s,(kg/m^3),	$1 \cdot 9 \ 10^3$

where Γ, H_1 and n are empirical constants, C_{vs} is the specific heat for pure solid, ρ_{s0}, T_{s0} and p_{s0} are the ambient density, temperature and pressure of the pure solid respectively.

The Jones–Wilkins–Lee (JWL) equation of state is used for gas-phase products of HMX and is of the form

$$e_g(p_g, \rho_g) = \frac{1}{\omega \rho_g}[p_g - (Ae^{C_1/\rho_g} + Be^{C_2/\rho_g})]$$

$$-C_{vg}T_{g0} - Q + \frac{1}{\phi_{s0}\rho_{s0}}\left[\frac{A}{R_1}e^{C_1/\rho_g} + \frac{B}{R_2}e^{C_2/\rho_g}\right], \tag{33}$$

where ω, A, B, R_1, R_2 are empirical constants, Q is a parameter to measure the detonation heat release, and C_1, C_2 are defined by $C_1 = -R_1\phi_{s0}\rho_{s0}$, $C_2 = -R_2\phi_{s0}\rho_{s0}$. The forms given in (32) and (33) were chosen to make our study consistent with those of the larger LANL-DDT group as recorded in [7, 19]. The EOS for the pure phases given above are used in the BKS and SVG models directly without modification. The constants are assigned only one set of values for all three models and are subsequently never changed in this study. In the GISPA model one uses the EOS shown in (31), where the functional forms e_s and e_g are the same as those given above.

We list in Table 1 the numeric values of the constants used in the EOS together with ambient properties.

4.2. THE COMPACTION PROCESS

It is found experimentally that if excess pressure is applied, then a bed of porous material will deform into a new average configuration with a new average value of the porosity, or new average state of compaction. It is common to assume that there exists an equilibrium compaction state for the bed that identifies an equilibrium compaction pressure P_{eqb} with a corresponding configuration state denoted ϕ_{eqb}. It is assumed that isothermal, quasi-static

compaction experiments define a $P_{eqb} - \phi_{eqb}$ response curve. If the curve goes through the point (p_0, ϕ_0), then we can represent the isothermal quasi-static response as

$$p_{eqb} = p_0 + \mathcal{P}(\phi), \tag{34}$$

where $\mathcal{P}(\phi)$ is often called the configurational stress. If we represent $\phi = V_s/V \equiv 1/\alpha$, then we can identify this curve as the so-called $P - \alpha$ law. Recently, Sheffield and Gustavson [20] used the following simple form for $\mathcal{P}$ (attributed to Hermann) to describe the quasi-static compaction of HMX

$$\mathcal{P}(\phi, P_h) = \begin{cases} P_h \left(1 - \sqrt{\dfrac{\phi_0(1 - \phi)}{\phi(1 - \phi_0)}} \right), & p - p_0 \leqslant P_h, \\ P_h, & p - p_0 > P_h. \end{cases} \tag{35}$$

The parameter P_h is called the hardening pressure, or consolidation pressure, beyond which material will crush to solid density. If we invert the above expression, we obtain the expression for $\alpha = 1/\phi$ as

$$\alpha = \begin{cases} 1 + (\alpha_0 - 1)(1 - p/P_h)^2, & p - p_0 \leqslant P_h, \\ 1, & p - p_0 > P_h. \end{cases} \tag{36}$$

To model dynamic compaction, the simplest assumption is that the material rate of change of the state variable that governs the compaction process is proportional to the difference between the average bed pressure p and the quasi-static equilibrium pressure $\mathcal{P}(\phi)$. This guarantees that the quasi-static equilibrium states are obtained at the conclusion of the dynamic transients. For the BKS model, the compaction process is controlled by the fraction of solid, say. Thus in expression (35) we replace ϕ by ϕ_s and then the compaction-rate function r_{ϕ_s} in the BKS model is taken as

$$r_{\phi_s} = k_{\phi_s}[p - p_0 - \mathcal{P}(\phi_s, P_h)] + (C_s^+/\rho_s). \tag{37}$$

In the SVG model, the decrease in the void fraction represents the compaction process. The volume of the solid relative to the volume of the porous solid would be calculated by $\phi = \phi_s/(\phi_s + \phi_v)$ and it is then substituted in (35). Thus, for the SVG model, the compaction-rate function r_{ϕ_v} is written as

$$r_{\phi_v} = k_{\phi_v}[p - p_0 - \mathcal{P}((\phi_s/(\phi_s + \phi_v)), P_h)], \tag{38}$$

where k_{ϕ_v} is a rate constant and p is the bulk pressure. Finally for the GISPA model, the compaction variable is represented directly by ϕ and we take the following form for the compaction rate function r_ϕ

$$r_\phi = k_\phi[p - p_0 - \mathcal{P}(\phi, P_h)]. \tag{39}$$

4.3. REACTION-RATE LAW

Next we turn to a discussion of the reaction-rate modeling. Especially for the experiments with relatively low piston velocities in the range from 50 m/sec $< u_{\text{piston}} <$ 100 m/sec, it is

thought that the reaction associated within the primary compaction wave can be attributed to a surface-burning mechanism of the grains [21]. Thus, the kinetics of the surface reaction that includes pyrolysis which is an autocatalytic reaction of the HMX-product gases evolved from the surface with HMX liquid, and the character of the damage and deformation on the surface of the grains, should play a role in the formulation of the appropriate lumped rate forms used in these DDT models. For example, to model the early induction period of the LANL-DDT-tube experiment, McAfee *et al.* [22] used a kinetic relation of the form

$$\frac{\mathrm{d}\lambda}{\mathrm{d}t} = k(\lambda + \alpha_0)^n (1 - \lambda)^m. \tag{40}$$

where λ denotes product concentration, α_0 is initial product concentration and k, n, m are constants.

The interpretation in the LANL experiments [11] has suggested that after the lapse of the first phase, where the compaction wave propagates with energy release in a form of slow surface burning which can be described consistently by (40), the detonation suddenly and promptly occurs and the reaction rate in the region where detonation originates suddenly increases beyond what could be predicted by kinetics used to describe the first slow phase. Also, it was found that prompt detonation occurred in the region of nearly full-density material (the plug) that had been previously processed by the lead compaction wave. Simple considerations and numerical modeling that retain only the slow rate [3] are inconsistent with the LANL experimental observations on detonation initiation; it does suggest however that relatively little reaction in the plug could be taking place in the first phase, prior to detonation.

We can possibly explain the rapid onset of detonation in the plug region by assuming that the kinetic mechanism used to model standard shock-to-detonation transitions (SDT) in full density explosives, is operating in the dense material. It is consistent with the experiments to assume that the slow reaction predominates in the region closest to the piston and serves as the source of energy that drives pressure waves into the denser material ahead. The material ahead of the combustion region near the piston further compacts, and eventually a secondary compaction wave or shock forms, which serves to further compress the dense, unreacted material. Thus, the rear interface of the plug between the combustion and the unreacted region acts as a piston that drives the shock running into the plug region. As the burning region expands, it strengthens the shock. When the shock pressure in the plug region reaches a threshold pressure of a full-density material, it can detonate in the unreacted region via an SDT-kinetics mechanism.

To model the SDT-kinetics mechanism, we assume that, if the material is sufficiently dense and if the density is below some threshold density, then the STD mechanism is absent or 'turned off'. If the density is above a threshold density, then the reaction rate is assumed to be a function of the shock pressure that the material first experiences. The pressure value is associated in the dense region with a material particle that is encountered by the pressure shock. Thus, material particles remember the strength of the secondary shock P_{shock} that first passes over sufficiently dense material, and such a pressure can be mapped to the particle's unique Lagrangian position.

We model the SDT-kinetics threshold with a switch indicator function that detects a sufficiently high density. (The kinetics are also off if the pressure is below some very low minimum pressure, and the pressure threshold effectively plays no role other than to keep the rate in barely disturbed material at zero). The switch is expressed as a Heaviside step function whose argument is the density, centered on a critical value of the density (95 % TMD, say).

The switch is 1 when the material density is above the threshold and is 0 otherwise. This switch is then multiplied by a non-zero rate expression. When the switch is on, the pressure P_{shock} is recorded and is assigned to the Lagrangian material particle label ξ. Subsequently, for a fixed Lagrangian particle, where the SDT kinetics is applicable, we assume that the rate is defined by an Arrhenius-like pressure-dependent function.

$$r_\lambda \equiv \frac{\text{D}\lambda}{\text{D}t} = k_2(1 - \lambda) \exp(-Ep_0/P_{\text{shock}}), \tag{41}$$

where k_2 is a rate constant, and E is an activation energy-like constant.

The density switch also serves to identify an internal phase boundary in the HMX material. At any point, if the density threshold is crossed, we record the location of the *rightmost* boundary of the dense material associated with the particular Lagrangian particle label ξ_s that corresponds to the Eulerian location $x_s = X(\xi_s, t)$ where $X(\xi_s, t)$ represents the Lagrangian trajectory of the ξ_s-particle. Thus we can track the locus of a secondary shock explicitly. Further, if we integrate the Lagrangian trajectories of the particles that pass through this *secondary-shock* locus, then we can fill a region of the x, t-plane at later times with these trajectories.

From an Eulerian viewpoint, at a fixed time and position (x, t), we can determine the shock pressure $P_{\text{shock}}(\xi)$ by simply identifying which particle trajectory has passed through that Eulerian point. We must have integrated the particle paths to find the Eulerian trajectories to do this, and the mapping between Lagrangian frame and Eulerian frame is required. Since path lines do not intersect, the mapping is isomorphic, (*i.e.* a one-to-one and onto mapping). Since the rate function in the plug region is assumed to be a function of the shock pressure P_{shock}, and since the secondary shock pressure P_{shock} is in turn a well-defined function of ξ, the rate function for the SDT kinetics is always a well-defined function of the particle label and can be computed unambiguously. The Lagrangian paths can be described as follows. First the particle trajectories are advanced for all particles. Let $X(\xi, t)$ be position function of a material particle ξ, that initially resides at $x = \xi$ at $t = 0$ (say). After each hydrodynamic iteration from t to $t + \Delta t$, the Eulerian velocity $u(x, t)$ is advanced and the new Eulerian position of ξ is then calculated by

$$X(\xi, t + \Delta t) = X(\xi, t) + \int_t^{t+\Delta t} u(X(\xi, \bar{t}), \bar{t}) \, \text{d}\bar{t}. \tag{42}$$

Now we discuss the specific implementation of the kinetics of exothermic reaction for the various models. For both the BKS and SVG models, we assume that reaction variable λ is the mass fraction of the gas and can be identified as

$$\lambda = \rho_g \phi_g / \rho. \tag{43}$$

In the GISPA model, λ simply represents a reaction progress variable. We define the density *switch* by

$$switch = \begin{cases} 1, & \rho \geqslant \rho_{\text{crit}}, \\ 0, & \text{otherwise}, \end{cases} \tag{44}$$

Table 2. Comparison of model variables, closure relations, equation of states, source terms and rate laws.

Definition	BKS	SVG	GISPA
Solid volume fraction	ϕ_s	ϕ_s	ϕ
Gas volume fraction	ϕ_g	ϕ_g	
Void volume fraction		ϕ_v	
Solid density	ρ_s	ρ_s	ρ/ϕ
Gas density	ρ_g	ρ_g	
Solid pressure	p_s	p_s	p/ϕ
Gas pressure	p_g	p_g	
Solid internal energy	e_s	e_s	e_s
Gas internal energy	e_g	e_g	e_g
Closure relation	$\rho = \phi_s\rho_s + \phi_g\rho_g$ $p = \phi_s p_s + \phi_g p_g$ $e = \frac{1}{\rho}(\phi_s\rho_s e_s + \phi_g\rho_g e_g)$	$\rho = \phi_s\rho_s + \phi_g\rho_g$ $p = p_g$ $e = \frac{1}{\rho}(\phi_s\rho_s e_s + \phi_g\rho_g e_g)$	ρ p e
Equation of state	Hayes (32) & JWL (33)	Hayes (32) & JWL (33)	combined (31)
Mass source term	$C_s^+ = -r_\lambda$ (45) (43)	$C_s^+ = -r_\lambda$ (45) (43)	
Energy source term	E_s^+ (11)		
Compaction law	r_{ϕ_s} (37)	r_{ϕ_v} (38)	r_ϕ (39)
Reaction law		r_λ (45), λ (43)	r_λ (45)

where ρ_{crit} is a constant. The region where *switch* = 1 defines the high-density region, and the rightmost boundary of the plug region. The kinetic rate expression for energy release, used for all three models, can now be written as

$$r_\lambda = H(p - P_{\text{ign}}) \begin{cases} k_1(\lambda + \alpha_0)^b(1 - \lambda), & (switch = 0), \\ k_2(1 - \lambda)\exp(-Ep_0/P_{\text{shock}}), & (switch = 1), \end{cases} \tag{45}$$

where $H(x)$ is Heaviside function and P_{ign} is a parameter. The parameters k_1, k_2, b, α_0, E are constants and p_0 is the ambient pressure.

In both the BKS and SVG models, we identify the mass source term C_s^+ as follows

$$C_s^+ = -cr_\lambda, \quad \text{where} \quad \lambda = \rho_g\phi_g/\rho. \tag{46}$$

But in the SVG model we *must* specify both source term C_s^+ and r_{ϕ_g} which can in principle be independent. We make the choice for the SVG model that $C_s^+ = -cr_\lambda$ and $r_{\phi_g} = r_\lambda$ and allow the constant c to represent possible independence of these terms.

4.4. SUMMARY

To illustrate the similarities and differences of the models, we tabulate in Table 2 the variables and constitutive forms used by each model. Since ρ, u, p, e, representing bulk density, bulk velocity, bulk pressure and bulk internal energy for all models repsectively, they are not listed in Table 2.

5. Model solutions calibrations and predictions

In this section, we discuss the solution procedure, the calibrations of the simulation to the LANL DDT-tube experiment and predictions of the models.

Table 3. Calibrated parameters in compaction study for the inert base case.

Parameter	BKS	SVG	GISPA
Porosity	$\phi_{s0} = 0.7$	$\phi_{v0} = 0.3$	$\phi = 0.7$
u_p (m/s)	100	100	100
P_h (Pa)	$1.2 \cdot 10^8$	$1.1 \cdot 10^8$	$1.0 \cdot 10^8$
Rate constant (kg/m/s)	$k_{\phi_s} = 20$	$k_{\phi_v} = 35$	$k_\phi = 32$

5.1. NUMERICAL METHOD

The DDT models presented in Section 3 vary from single to three phase with five or six as the number of governing equations and are posed in both conservative (the SVG and GISPA models) and non-conservative (the BKS model) formulations. Moreover, the equations of state assumed by all models are non-ideal. Thus we decide to use McCormack's method, which is a predictor-corrector finite-difference scheme with second-order accuracy in space and time, since it can easily handle non-ideal EOS forms and can be implemented in a straightforward way. We integrated the source terms, using the Strang splitting which gives second-order accuracy with the explicit frozen-state calculation as suggested in [23]. The source-term calculation is subcycled at every hydrodynamic time step to resolve fast evolving chemistry. While high-resolution Godunov-type schemes ([24, 25]) lead to higher accuracy and are attractive, specific treatment for solution of the non-ideal Riemann problem is required [26] and these methods are somewhat more difficult to implement.

For convenience, the computations are carried out in the piston frame, where the ambient material moves toward the piston. The standard computational domain we used has a physical size of approximately 100 mm which we discretize by using approximately 2000 grid points. The CFL condition was used to control the time-step size and ranged from 0.4 to 0.8. Numerical viscosity was added to the solver to increase the stability of the method at shocks. We implemented the regularization in the BKS model, using nonlinear artificial viscosity in which the viscosity was added to the flow field where it is not smooth [17]. A reflective boundary condition was used at the left boundary and an outflow boundary condition [27] was applied at the right boundary. the GISPA model was solved with the code AUGUST which is described further in [3]; the SVG model was solved with the code SEPTEMBER-SVG and the BKS model by the code SEPTEMBER-BKS. The SEPTEMBER code is a descendent of AUGUST, which was jointly developed by the authors, J. Bdzil and S. Son at Los Alamos and A. Kapila at Rensselaer Polytechnic Institute for the LANL-DDT Program.

5.2. INERT COMPACTIONS STUDIES

We carried out detailed inert compaction-wave simulations first in order to set the parameters that govern the material strength of the inert porous material and to verify the numerical solution of the model governing equations, before conducting reactive simulations. In the inert case (no reaction), all three models are simplified. In particular, an analytic solution for the structure of a steady traveling compaction wave can be derived simply for the conservative model GISPA. We simply integrate the mass, momentum and energy equation and evaluate the resulting constants in the ambient material. This is equivalent to carrying out the Rankine-Hugoniot analysis where the density, particle velocity and pressure are determined as explicit functions of the compaction variable. Then these forms are inserted into the compaction-rate
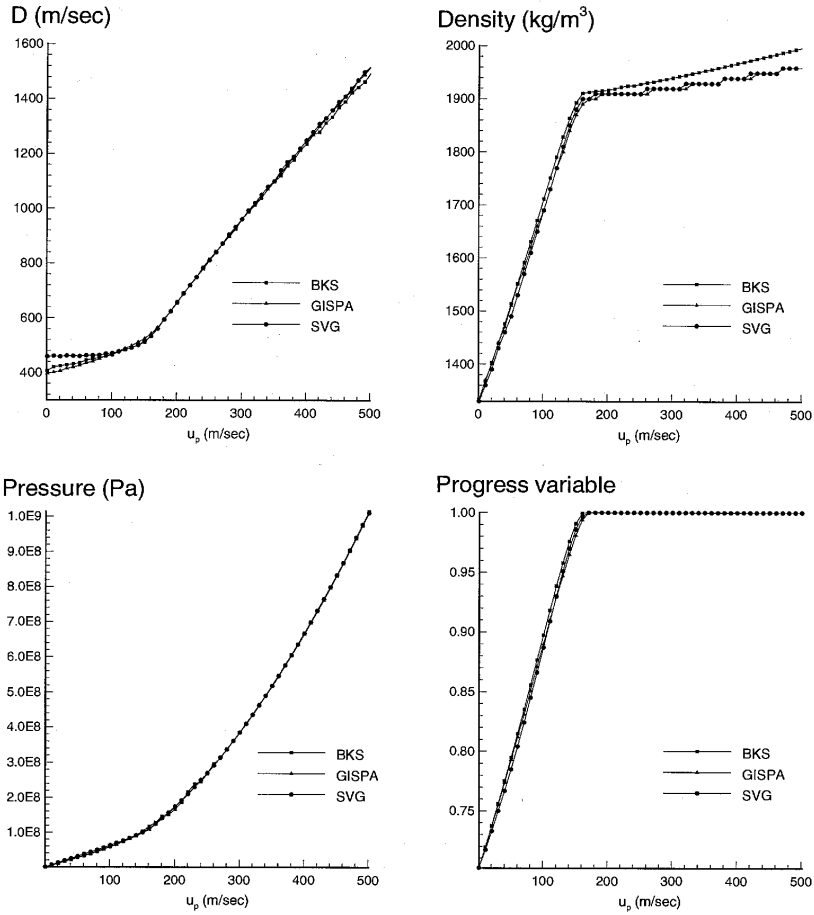
Figure 6. Comparison of inert compaction-way properties: speed and end states versus piston velocity for the base case used in the calibration. Results for all three models are shown. The compaction variable for the BKS model is ϕ_s, for the SVG model it is $1 - \phi_v$ and ϕ for the GISPA model.

equation which is integrated to obtain the variation of compaction; hence the other dependent variables can be determined as functions of distance in the wave coordinate. The profiles of an inert compaction wave as obtained from the code can then be compared with the analytical solution as a check. The only experimental information that we used to calibrate the compaction wave was that we assumed that the compaction-wave thickness was 2 mm for a piston-impact velocity of 100 m/sec in a 70 % TMD material and that the resulting compaction wave runs at about 425 m/sec in the laboratory frame, which is typical in the experiments. We refer to this as the inert base case.

The inert base case is characterized by the absence of energy release; thus, we set $r_\lambda = 0$ and $C_s^+ = 0$. Only two parameters in the compaction-rate function are determined by calibration for all models. The rate constants $k_{\phi_s}, k_{\phi_v}, k_\phi$ were chosen to calibrate the thickness of the compaction wave and the hardening pressure P_h in (37), (38) and (39) was chosen to calibrate the speed of the compaction wave to the base case. The calibrated parameters are listed in Table 3.

Once the parameters were fixed, the end state of density, pressure and compaction progress variable, together with wave speed, could be determined as functions of input piston velocity

as shown in Figure 6. All three models predict similar equilibrium compaction-wave end states, with small variations. Thus, parameters can be found for all three models, such that their predictions for the inert base case are essentially identical.

5.3. CALIBRATION OF REACTION KINETICS

Having determined parameters required to describe inert compaction, we now turn into the calibration of parameters in reaction law, defined by (45). The ignition pressure threshold was set to the low value $P_{\mathrm{ign}} = 1 \cdot 0 \cdot 10^7$ for all models and was not changed. What was left was to determine the reaction-rate constants k_1 and k_2, the exponent b, the initial product concentration α_0, for the slow burning kinetics and activation energy-like constant E.

To carry out the calibrations, we used the following experimentally observed features in the LANL experiment as a guide:

(1) The elapsed time to the appearance of secondary shock which is taken to be the time to plug formation and labeled t_{shock};
(2) The elapsed time to detonation, denoted t_{det}, and
(3) The observed detonation speed after ignition of detonation D. For example, in experiment E-5586, the elapsed time to appearance of secondary shock is about 110 μsec and time to detonation is about 170 μsec. The detonation speed immediately after ignition is 6·16 km/sec. The same data associated with the events in the experiment can be obtained from the numerical simulation.

The time to detonation and time to appearance of secondary compaction were defined precisely in the simulation by inspection for each model of the contour plot in the x-t plane of the density. Complete compaction or the loss of void sends out a secondary compaction wave which can be recognized as a jump in density profile, and it is a simple matter to record t_{shock} as the time of the first appearance of the jump associated with the secondary shock. Similarly, t_{det} is defined when a much stronger shock is generated by the rapid change in the reaction rate of the SDT kinetics. This phenomena can be identified in the density profile as a sharp jump followed by a rapid density combined with the appearance of the classical detonation profile that is observed in all the simulations. The slope of the locus of the detonation shock in the x-t plane determines the detonation speed.

The procedures used in the calibration of the kinetics constants are described next. The initial product concentration α_0 is taken to be small, (less than $1 \cdot 0 \cdot 10^{-5}$) which is the assumption made by McAfee *et al.* in their autocatalytic reaction rate model [22]. The rate constants k_1 and the exponent b that appear in the slow kinetics are adjusted, so that the model simulations match the time of appearance of secondary shock. The activation energy-like constant E is adjusted to match the time to detonation t_{det}. Finally, the rate constant k_2 is adjusted to match the detonation speed after ignition. The primary goal in the calibration is to adjust the time to detonation. The changes in the simulation on the detonation speed observed are very weak, but are associated with the fact that the detonation is still not a steady wave. Thus, there is some slight effect associated with changing k_2. If the wave were absolutely steady, there would be no dependence of the final speed on k_2. If choice of the slow phase kinetics parameters α_0, k_1 and b do not predict correct time to detonation, (*e.g.* suppose the induction time is too short which results in an early transition), then those constants were changed to meet the time-to-detonation requirement.

Table 4. Calibrated compaction and reaction parameters for the base case.

Parameter	BKS	SVG	GISPA
Porosity	$\phi_{s0} = 0.7$	$\phi_{v0} = 0.3$	$\phi = 0.7$
P_h (Pa)	$1.2 \cdot 10^8$	$1.1 \cdot 10^8$	$1.0 \cdot 10^8$
Compaction rate constant (kg/m/s)	$k_{\phi_s} = 20$	$k_{\phi_v} = 35$	$k_{\phi} = 32$
α_0	$1.0 \cdot 10^{-6}$	$1.3 \cdot 10^{-6}$	$2.5 \cdot 10^{-8}$
b	1.0	1.1	1.04
k_1 (kg/m/s^3)	$5.0 \cdot 10^7$	$2.5 \cdot 10^8$	$2.3 \cdot 10^8$
k_2 (kg/m/s^3)	$9.0 \cdot 10^9$	$6.0 \cdot 10^9$	$6.5 \cdot 10^9$
E	$3.0 \cdot 10^4$	$1.2 \cdot 10^4$	$6.6 \cdot 10^4$

The calibrated compaction and energy-releasing kinetics parameters are listed in Table 4. In the next section we describe the detailed comparisons between the predictions of the simulations of the three models and the comparisons with the LANL experiment.

5.4. MODEL COMPARISONS WITH SHOT E-5586

For what we now refer to as the base case, we assumed that $u_p = 100$ m/s and that the initial porosity correspond to 70 % TMD. Figure 7 shows x-t plots of experimental record from shot E-5586 and the calibrated simulations from the three DDT models. The different, distinct loci that correspond to the experimentally measured fronts are shown and diagrams are plotted at the same scale as in the lab frame. The plots are arranged so that the elapsed time starts when the compaction wave has propagated approximately 41 mm from the piston to match with the plot from E-5586. Note that the discrepancy in absolute time is due to a transient in the DDT tube associated with the early acceleration of the piston driven by the burn chamber. Other features of the model simulations are shown for comparison in Figures 8 and 9; the spatial profiles of density and log pressure (measured in Pascals), respectively, at two distinct times $t_1 = 160$ μsec and $t_2 = 174$ μsec are shown. The times t_1 and t_2 are the times before and after the transition to detonation.

Model predictions of the SVG and GISPA models are in strong qualitatively agreement and show differences when compared against the BKS model. For the SVG and GISPA models, after the impact of the piston with the porous bed, a compaction wave labeled c in the graphs runs into the unreacted material at about 430 m/sec. The early compaction process is almost inert. The mass fraction of gas is in a range from $3.0 \cdot 10^{-6}$ to $1.0 \cdot 10^{-4}$ behind the primary compaction front and the bulk variables in the compacted material are close to those found for the equilibrium inert compaction state. After the end of an induction period, combustion starts vigorously near the piston interface and the region of energy release expands into the compacted material. The locus of the burning front, labeled b in the graph, is a contour of constant mass fraction of gas with the value of roughly order 0.1, (0.08 for the SVG model and 0.09 for the GISPA model).

As a result of the early combustion, the secondary shock is formed shortly after the burning front b moves away from the piston face. The shock front, labeled s, propagates faster than the boundary of the combustion region and propagates into the compressed inert material. The locus of the secondary compaction shock can be seen clearly as a jump in density profile for
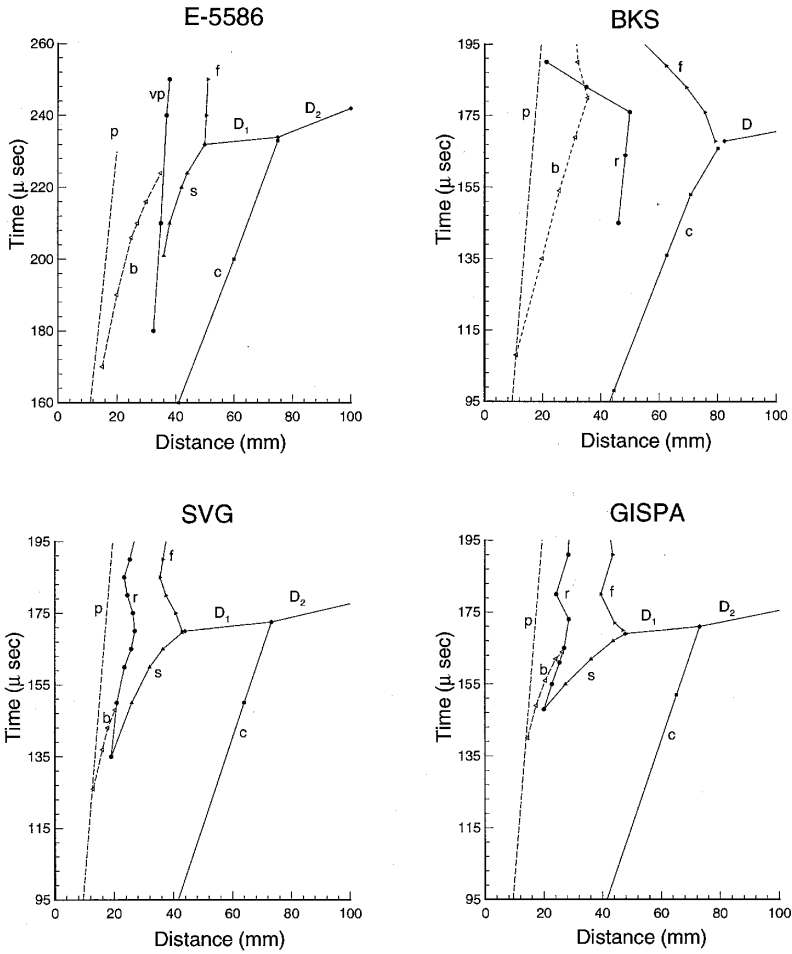
Figure 7. A side-by-side comparison of the x-t plots of the experimental record from shot E-5586 and the calibrated simulations of each of the three DDT models. Notation: u_p, piston velocity; c, compaction; b, burning front; r, rear of the plug, or the virtual piston; s, secondary shock; D_1 and D_2, detonation; f, front of the plug.
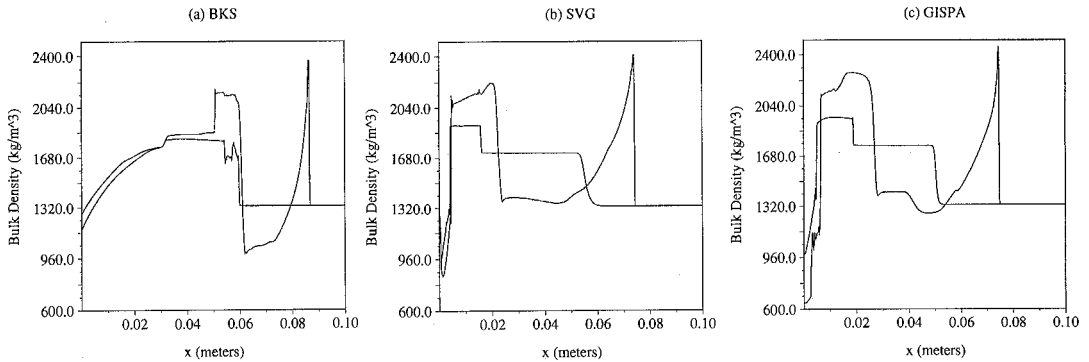

Figure 8. A comparison of the bulk density profiles of the three models slightly before ($t_1 = 160$ μsec) and after ($t_2 = 174$ μsec) the initiation of detonation.
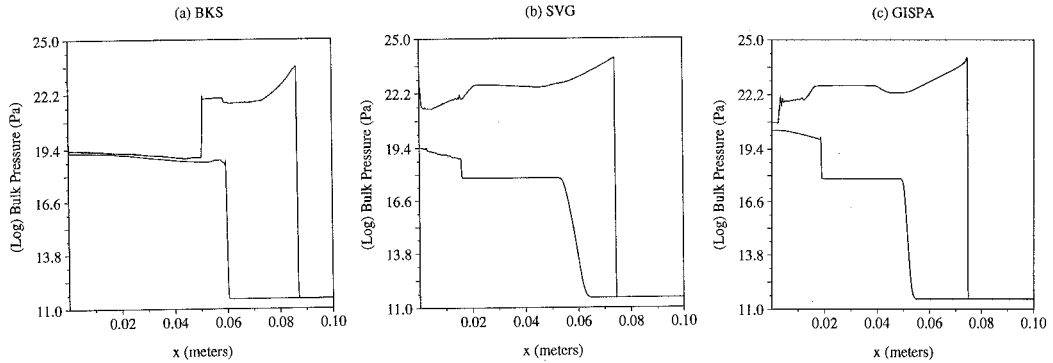
Figure 9. A comparison of the profiles of log (P) where P is measured in Pascals, for the three models slightly before ($t_1 = 160$ μsec) and after ($t_2 = 174$ μsec) the initiation of detonation.
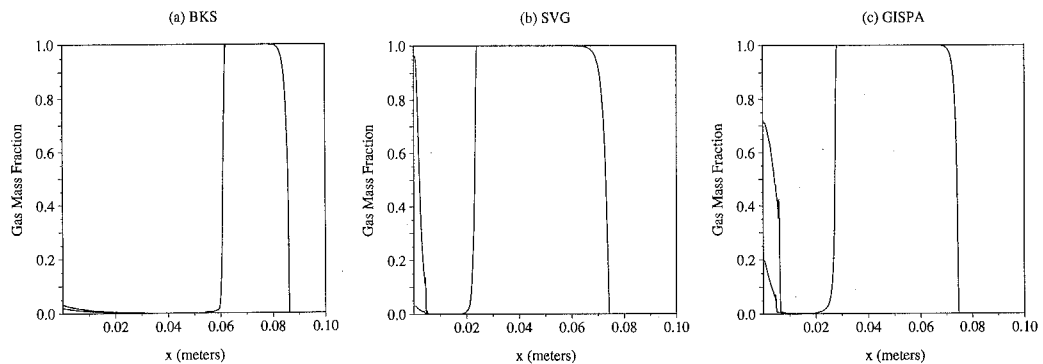

Figure 10. A comparison of the profiles of gas-mass fraction for the BKS and the SVG models and the reaction progress variable λ for the GISPA model slightly before ($t_1 = 160$ μsec) and after ($t_2 = 174$ μsec) the initiation of detonation.

the SVG and GISPA models, (see Figures 8(b) and 8(c)) and it also can be identified exactly by the locus $\phi_v = 0$ in the SVG model and $\phi = 1$ in the GISPA model.

Passage of the secondary compaction shock further compacts the material to about 100 % TMD. The high density is maintained at a near constant value behind the shock front, until it is encountered by the combustion front b, where the density drops sharply as indicated in Figures 8(b) and 8(c). The contours of a high-density value right before its rapid decline identify an interface, labeled r, as shown in Figures 7(c) and 7(d) (between the completely compacted material and the porous material on the other side). The highly condensed material, between loci s and r, is the plug. And loci r in the simulations correspond to vp in the experiment (see plot E-5586 of Figure 7(a)).

For the SVG and GISPA models, there are two striking features associated with the plug. First, the plug is dense and hence is relatively cold; little reaction takes place in it. Figures 10(b) and 10(c) show that, before the transition, the mass fraction of gas is almost zero inside the plug for all models. Second, the pressure buildup at the front of the plug, immediately behind the secondary compaction shock prior to the ignition of the detonation, is exponential and eventually triggers the STD kinetics implemented in our models. Evidence of a pressure build-up behind the secondary shock has been argued for in the context of the interpretations of the experiments [11]. As a consequence of the rapid pressure increase behind the secondary

Table 5. Comparison of DDT properties from the experiment and the simulation
for the base case.

Property	E-5586	BKS	SVG	GISPA
Compaction speed (m/sec)	424	465	430	427
Detonation speed, D_1 (km/sec)	–	–	6·5	6·7
Detonation speed, D_2 (km/sec)	6·16	6·0	6·2	6·25
Density in plug before detonation (g/cc)	1·94	1·83	1·93	1·95

shock, the detonation initiates at the front of the plug, adjacent to material that has been processed only by the primary compaction wave, immediately in front of it. The detonation speed is approximately 6400 m/sec in the material processed by the primary compaction wave (denoted as D_1) and later travels about 6100 m/sec in the fresh material (denoted as D_2) in the simulations of both the SVG and GISPA models.

The newly ignited detonation causes a pocket of material in close vicinity of the detonation shock to proceed rapidly to complete reaction and leaves a residual of unburnt material behind in what was the unreacted plug. The pressure rise form the ignition of the detonation pushes the plug backward towards the piston. The interface between the plug and product gas is formed at the time of detonation ignition and the locus of the interface at the front of the plug is labeled f in Figures 7(a) and 7(d). The observation of a long-lived residual plug is also recorded in the LANL experiments. Note that the experimental record does not accurately determine the trajectory of the plug residual past the time of the ignition of the detonation [28] and that there may be a retonation and motion of the plug backwards towards the piston.

A qualitatively different detailed scenario is observed in the simulation of the BKS model. A major difference is in the formation of the secondary shock. In the simulations, the density rises to about 96 % TMD before the detonation, but an obvious, sharp density variation between regions of primary and secondary compaction is not observed in the compacted material. Instead, the BKS model predicts the highest density near the head of the primary compaction wave. The secondary shock front, if it can be distinguished as a separate front at all, is observed to follow closely the primary compaction front. Since we observed no distinct jump in density (see Figure 8(a) at time $= t_1$), a separate locus (s) is not shown in Figure 7(b). However the compaction front did accelerate in the simulation (from roughly 430 m/sec at $t = 20\mu$ second to approximately 500 m/sec at $t = 150\mu$ second) and the ignition of detonation occurred right in front of the primary compaction wave. Since detonation triggers near or at the head of the primary compaction wave, the detonation initially runs into fresh material and there is no distinction between D_1 and D_2 as there is for the SVG and GISPA models. After ignition of detonation, the BKS model shows clear evidence of a retonation wave that pushes the front of the plug back towards the piston. The effect of the retonation is more pronounced in the simulation of the BKS model than in that of the other two models.

Another qualitative difference in the predictions of the BKS model and those of the SVG and GISPA models is associated with the amount of energy release prior to ignition. If we chooses kinetics parameters for the BKS model that strengthen the reaction of the slow-phase kinetics, then the primary compaction-wave locus (c), shown in Figure 7(b), becomes highly curved in the x-t plane which is associated with an accelerating primary compaction wave. This is in contrast to a primary compaction wave that has nearly constant velocity, which seems to be consistent with the experiment as shown in Figure 7(a). The reaction contour

labeled (*b*) in Figure 7(b) corresponds to a gas-mass fraction on the order of 0·01 (exactly 0·007) and is located roughly in the same positions as the like-labeled contours shown for the SVG and GISPA models, which reflect approximately 10 times more reaction. For the BKS model, the material that we would consider to be the plug is shown in Figure 7(b) to reside between the loci (*r*) and (*c*).

The lack of the appearance of a distinct secondary shock and the difficulty in maintaining a nearly constant-speed primary compaction wave, is likely a direct consequence of the BKS-model structure. Note that for the BKS, BN and similar models, the internal state variable ϕ_s for the solid-volume fraction always has the double duty of both representing the state of compaction and the state of reaction at the same time. The BKS model does not allow these rate processes to be truly independent. It is possible to add more ingredients to the BKS model, such as an extra degree of freedom as those equivalent to the BN kinetics model, to improve the prediction, but that would violate the premise of our original objective of the study, that is to give like information to all models in the simplest way possible. Our results suggest that it is probably inadequate to make correct predictions of transition to detonation with a model that has only one degree of freedom available to control both reaction and compaction.

We summarize the properties of the base-case DDT simulation for all models and the corresponding data from the LANL experiment in Table 5.

5.5. PREDICTION OF THE POP-PLOT DATA FROM THE MODEL KINETICS

After having calibrated the reactive base-case kinetics for the three models, we carried out run-to-detonation simulations for fully dense materials (initially at 100 % TMD) to compare against the PoP-plot data in dense HMX. In the standard run-to-detonation experiment the explosive is shocked, and distance from the boundary of the explosive material to the appearance of a detonation in the explosive is measured and plotted as a function of input pressure. The log-log plot of data is referred to as a PoP plot. Our objective was to check for consistency of the kinetics model obtained in Section 4.3 with the parameter set from the calibration of the reactive base case. The SDT kinetics should be able to reproduce the experimental data that records the shock initiation sensitivity for full density HMX [10].

To carry out this check, we first established the relationship between the piston velocity and the inert compaction-state pressure, since the initial condition for our simulations is prescribed in terms of the piston velocity. A Rankine-Hugonoit analysis similar to the compaction study can be carried out, or the code can be used directly to run an inert simulation, to obtain the relation between u_p and the shock input pressure. Thus we were able to construct a table of steady compaction-state pressures versus the piston velocity for pressures varying from 5 GPa to 10 GPa. The corresponding input piston velocity u_p was read off from the table. Then the simulation was run for u_p in the given range with initial porosity being set effectively to 1·0, which corresponds to bulk density of 1·891 g/cc used in [10]. All other parameters remained the same as the previously calibrated values.

The time scale of the PoP plot simulation is much smaller than that for the DDT tube simulation. It took less than 3 μ seconds of simulation time for detonation to reach the steady state for all piston velocities in the experimental range. The determination of the transition point, *i.e.* the run distance, made use of data from three categories: (a) the shock-
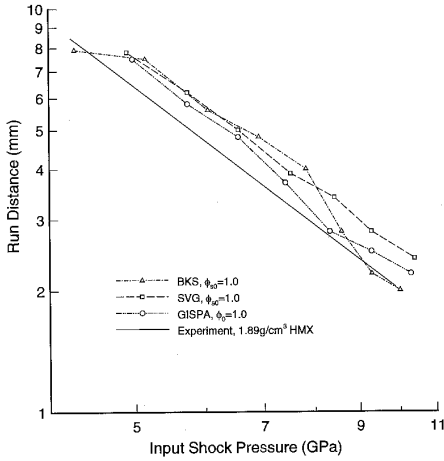
Figure 11. Run to detonation versus pressure (PoP-plot) for the three models initially at full density, compared with data from Dick [10].
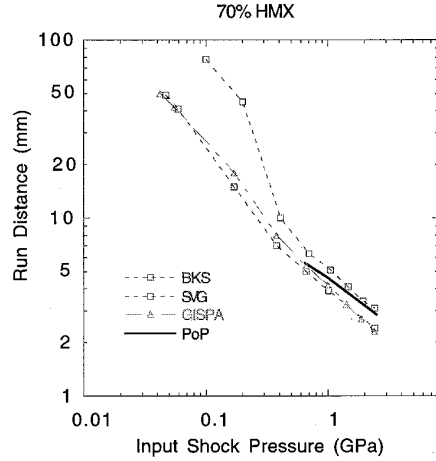
Figure 12. Run to detonation versus pressure (PoP-plot) for the three models initially at 70 % TMD, compared with data from Dick [10].

wave speed, (b) the shock-front pressure and (c) the end-state pressure. We assumed that the detonation we were attempting to observe would correspond to a steady-state wave in terms of wave speed, front value and end-state values for a given u_p. We determined the run-to-detonation distance by first finding the spatial point where the three data sets reached their steady-state values (99.5 % of their steady values). By matching the three data sets instead of one simple measure, we insured the reliability of the measurement. Figure 11 shows a comparison of PoP plots obtained by simulation from all three models against the experimental data of Dick [10]. (The good agreement is even more striking when plotted on a linear scale). All three models match the experimental data very well, which is a strong support for the consistency of the kinetics model that we adopt earlier.

Similar to the procedure used to make the PoP plot for full dense HMX, we also carried out the simulation of the three models for low-density HMX at 70 % and the result is plotted together with the experimental data from [10] in Figure 12. While the experiment was limited to a range where the impact shock pressure is between 0·6 and 2·5 GPa, we extended in the simulation the lower limit of the pressure to 0·055 GPa which corresponds to roughly $u_P = 100$ m/sec in our models. It is seen that for the input stress beyond 0·6 GPa, the predictions from all three models agree fairly well with the experimental. For the lower input pressures, the BKS model predicts a much longer run distance than that obtained from the SVG and GISPA models. The trend of the prediction for porous HMX is consistent with another simulation presented next.

5.6. PREDICTION OF RUN-TO-DETONATION DISTANCE VERSUS INITIAL POROSITY

Another prediction that can be made with our models is the run-to-detonation distance, or run distance, as a function of porosity of the material. The same physical experiments conducted by Russian scientists using PETN was introduced in Section 1. It is assumed that the response of granular HMX would be very similar to that of PETN according to [28]. Again, as mentioned in Section 2, we use the data for $\phi \in (0\cdot4, 1\cdot0)$ for a reliable comparison.

In the simulations, all the parameters were fixed to those that we decided on for the reactive base case, except porosity variables (ϕ_{s0} in the BKS and SVG model, ϕ in the GISPA
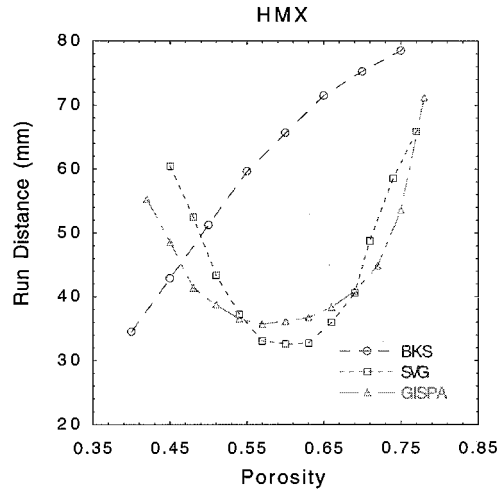
Figure 13. Run to detonation versus initial porosity (PoP-plot) for the three models initially at 70 % TMD.

model) which are varied from 0·4 to 0·8. Unlike the simulation of the PoP plot in 100 % TMD HMX, there is an obvious abrupt ignition associated with a distinct pressure jump when the detonation ignites in the porous material. We determined the run-to-detonation distance by checking for the first appearance of a detonation pressure. Then the distance from the high-pressure spot to the end of the tube is measured. The threshold pressure was 15 GPa. The run-to-detonation curves so produced are plotted in Figure 13. Again, it is found that the BKS model has a qualitatively different response from that of the SVG and GISPA models in that, as the porosity is varied, the run distance is monotonic, not U-shaped. The BKS model initiates early for higher porosity and later for lower porosity. In contrast, the SVG and GSIPA models predict U-shaped curves as the initial porosity is varied. The run to detonation has a minimum distance of about 35 mm at a compaction of around 0·55 to 0·6. The simulations in the SVG and GISPA models qualitatively match the response shape of the Russian experiments in PETN shown in Figure 4. We found in the simulations that for bed porosity lower than 0·4, detonation initiation did not occur. Compaction pressures are also lower as compared to those for larger porosity cases. This observation agrees with the physical scenario seen in low density DDT experiments.

6. Conclusions

In this paper, three reactive flow models for porous energetic materials are compared with the aim of finding the differences between the models in predicting basic DDT-related experiments. The BKS model is a two-phase, single-velocity model developed in [7, 14, 19] by asymptotic reduction from the BN model which was based on two-phase mixture theory. The SVG is a single-velocity, three-phase-formulation model with a different pressure-equilibrium closure. A void phase is introduced in the SVG model and is used as a device to model compaction as an independent rate process, The BKS and SVG models both adopt a common binary-mixture-theory viewpoint. The GISPA is a single-phase hydrodynamic model that requires the specification of a non-ideal equation of state in which reaction and compaction are assumed to be independent thermodynamic state variables.

Given that the models are structurally different in their derivation, we tried to use the same functional forms for the equation of state and compaction and reaction kinetics sub-models for the required constitutive theory in order to make a direct and quantitative comparison among model simulations. Moreover, in order to keep the mathematical structures unchanged from that of the original model-governing equations, we do not allow extra evolution equations to be added to the models in any way. Under these restrictions, we found that inert compaction can be modeled identically with all the models. Dramatic differences appear when reaction is included. We applied the same energy-releasing kinetics for all models, which uses a slow rate in porous material to model autocatalytic combustion on the surfaces of the grains and a faster shock-state-dependent kinetics to model SDT in condensed material. We showed that if we calibrate the parameters of the energy-releasing kinetics to match the base case of the DDT event (LANL-DDT-tube test E-5586), apparently we can model full density SDT shown by the agreement with the experimental PoP-plot data in [10].

Detailed comparison of the simulations of the SVG and GISPA models show both qualitative and quantitative agreement with LANL experiment. Features that are well simulated include the primary compaction wave, compaction induced combustion, prompt ignition of detonation, the formation of the plug and long-lived plug residual. Predictions of run-to-detonation distance in porous HMX by variation initial porosity also compare qualitatively well with available experimental data for PETN. One conclusion is that the BKS model as presented in this work probably needs another degree of freedom available to it in its rate modeling in order to reproduce the LANL experiments and to achieve the same level of agreement as with the SVG and GISPA models.

One motivation for this study was to identify a model that is suitable for high-quality multi-dimensional direct numerical simulation of DDT. Comparison across the models suggests that the single-phase GIPA model and the quasi-single-phase SVG model might be good candidates. They appear to be physically predictive and can consistently predict trends of DDT events as the porosity is varied. The GISPA model is the simplest model of all three with only five state variables. The SVG model would seem to predict best the features of the LANL experiment under the rules of comparison adopted by this study. Both the SVG and GISPA models are conservative, which is certainly an advantage for the implementation of high-quality shock-capturing numerical methods. Implementation of these contemporary methods, such as high-order ENO and TVD schemes, requires a mathematically simple and conservative model. Such a model could offer reduced computational cost which in turn could allow greater spatial resolution for predictive simulations.

Nomenclature

ρ	density;	C^+	mass source term;
u	velocity;	E^+	energy source term;
e	specific internal energy;	ϕ	volume fraction;
p	pressure;	λ	reaction progress variable;
T	temperature;	ξ	material particle;
P_s	pressure, used in reaction kinetic model;	s, g, v	subscript, indicating that the associated
r	rate function, for compaction or reaction;		variable is a solid, gas or void-phase
V	volume of material;		variable respectively.

References

1. M. Baer and J. Nunziato, A two-phase mixture theory for the deflagration to detonation transition (DDT) in reactive granular materials. *Int. J. of Multiphase Flow* 12 6 (1986) 861–889.
2. J. M. Powers, D. S. Stewart, and H. K. Krier, Analysis of steady compaction waves in porous materials. *J. of Appl. Mechanics* 56 (1989) 15–24.
3. D. S. Stewart, B. Asay and K. Prasad, Simplified modeling of transition to detonation in porous energetic materials. *Phys. of Fluids* 6 (1994) 2515–2534.
4. K. K. Kuo, R. Vichnevetsky and M. Summerfield, Theory of flame front propagation in porous propellant charges under confinement. *AIAA Journal* 11 (1973) 444–451.
5. P. B. Butler and H. Krier, Analysis of deflagration to detonation transition in high-energy solid propellants. *Combustion and Flame* 36 (1986) 31–48.
6. J. Bdzil and S. Son, *Deflagration-to-Detonation Transition*, LA-12794-MS, Los Alamos National Laboratory (1994) 87 pp.
7. J. B. Bdzil, A. K. Kapila, R. S. Menikoff, S. F. Son and D. S. Stewart, Towards a new two-phase model of DDT, Part I: Review of modeling issues. Submitted to *Phys. of Fluids* (1996).
8. B. W. Asay, S. F. Son and J. B. Bdzil, The Role of gas permeation during convective burning of granular explosives. *Int. J. of Multiphase Flow* 22 (1996) 923–952.
9. E. M. Kober, J. B. Bdzil and S. Son, Modeling DDT in granular explosives with a multi-dimensional hydrocode. Proceedings of the Conference of the American Physical Society Topical Group on Shock Compression of Condensed Matter, Seattle, WA, AIP Press (1995) 437–440.
10. J. J. Dick, Measurement of the shock initiation sensitivity of low density HMX. *Combustion and Flame* 54 (1983) 121–129.
11. J. M. McAfee, B. Asay, W. Campbell and J. B. Ramsay, Deflagration to detonation in granular HMX. *Ninth (Int.) Symp. on detonation* 1 (1989) 265–279.
12. S. Son, B. Asay and J. B. Bdzil, Inert plug formation in the DDT of granular energetic materials. Proceedings of the Conference of the American Physical Society Topical Group on Shock Compression of Condensed Matter, Seattle, WA, AIP Press (1995), 441–444.
13. A. I. Korotkov, A. A. Sulimov, V. Obmenin, V. F. Dubovitskii and A. I. Kurkin, Transition from combustion to detonation in porous explosives. *Fizika Goreniya i Vzryva* 5 (1969) 351–325.
14. J. B. Bdzil, A. K. Kapila, R. S. Menikoff, S. F. Son and D. S. Stewart, Towards a new two-phase model of DDT, Part III: Structure of the velocity-relaxation zone in the Baer–Nunziato model. Submitted to *Phys. of Fluids* (1996).
15. S. Son, Comments on the large-drag reduction of the Baer–Nunziato (BN) model. Private communication.
16. A. K. Kapila, Derivation of the BN model. Private communication.
17. S. Son, Regularization of the BKS model in the September code and the effect of artificial viscosity on the numerical integration of two phase equations. Los Alamos National Laboratory Memorandum (1995).
18. M. M. Carroll and A. C. Holt, Static and dynamic pore-collapse relations for ductile porous materials. *J. of Appl. Phys.* 43 (1972) 1627–1636.
19. J. B. Bdzil, A. K. Kapila, R. S. Menikoff, S. F. Son and D. S. Stewart, Towards a new two-phase model of DDT, Part II: Large-drag model and numerical simulations. Submitted to *Phys. of Fluids* (1996).
20. S. A. Sheffield and R. L. Gustavsen, Unreacted Hugoniots for porous and liquid explosives. *Proceedings of the Joint Air APT/APS Conference* (1993).
21. S. C. Li and F. A. Williams, Effective of Two-phase flow in a model for nitramine deflagration. *Combustion and Flame* 80 (1990) 329–349.
22. J. M. McAfee, B. W. Asay and J. B. Bdzil, deflagration to detonation in granular HMX: Kinetics and ignition in the predetonation region. *The Tenth Int. Detonation Symp.* (1993) 716–723.
23. P. Colella, J. Majda and V. Roytburd, Theoretical and numerical structure for reacting shock waves. SIAM *J. Scient. Stat. Comp.* 7 (1986) 1059–1080.
24. R. J. Le Veque, High resolution finite volume methods on arbitrary grids via wave propagation. *J. of Comp. Phys.* 78 (1988) 36–63.
25. A. Harten and S. Osher, Uniformly high-order accurate nonoscillatory schemes. *SIAM J. Num. Anal.* 24 (1987) 297–309.
26. P. Glaister, An approximation linearised Riemann solver for the Euler equations for real gases. *J. Comp. Phys.* 74 (1988) 382–408.
27. K. Thompson, Time dependent boundary conditions for hyperbolic systems *J. Comp. Phys.* 68 (1987) 1–24.
28. B. Asay, Run to detonation experiments for HMX materials. Private communication.